# Journal of Materials Chemistry A

Accepted Manuscript


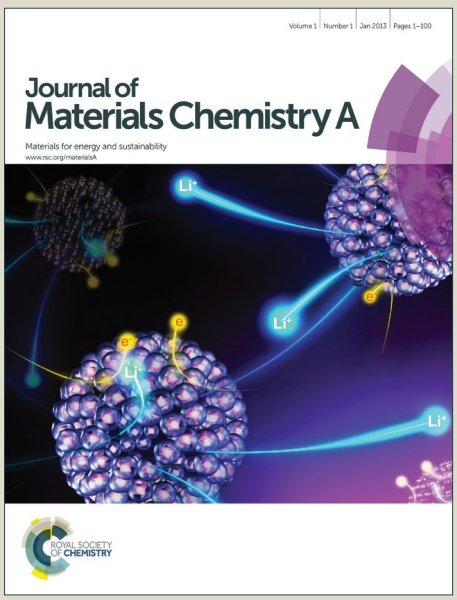





ROYAL SOCIETY OF CHEMISTRY

www.rsc.org/materialsA

Cite this: DOI: 10.1039/c0xx00000x

www.rsc.org/xxxxxx

ARTICLE TYPE

# Mechanism analysis of the capacitance contributions and ultralong cycling-stability of the isomorphous $MnO_2$@$MnO_2$ core/shell nanostructures for supercapacitors

**Jiajia Shao,[a] Xiying Zhou,[a,]* Qian Liu,[b] Rujia Zou,[b,c] Wenyao Li,[a,b,]* Jianmao Yang[b] and Junqing Hu[b,]***

***Received (in XXX, XXX) Xth XXXXXXXXX 20XX, Accepted Xth XXXXXXXXX 20XX***
**DOI: 10.1039/b000000x**

A facile method to synthesize isomorphous $MnO_2$@$MnO_2$ core/shell nanostructures was developed for the first time by using $MnO_2$ nanowires as seed crystals. Such unique nanoarchitectures consisting of an isomorphous layer of $\beta$-$MnO_2$ nanosheets well grown on the surface of $\beta$-$MnO_2$ nanowires exhibit remarkable electrochemical performance with high capacitance and ultra long cycle life, *i.e.*, nearly 92.2% retention after 20000 cycles at a current density of 5 A/g. The enhanced specific capacitanc of the $MnO_2$@$MnO_2$ electrode is largely contributed by the capacitive processes including double-layer charging and Faradaic pseudocapacity. Particularly, these intriguring behaviors are strongly correlated with the unique isomorphous core/shell hierarchical configuration and high mechanical stability as well as the better interfacial structures between the $MnO_2$ nanowire core and the ultrathin $MnO_2$ nanosheet shell. In addition, it is demonstrated that the formation of defective and disordered regions throughout the whole core/shell architectures are the main cause for the unusual increased capacity during the early stages of cyclic charge/discharge.

## 1. Introduction

Over the past few years, $MnO_2$ has been exploited as a cathode material used in lithium-ion batteries and fast charging materials for electrochemical capacitors (ECs) which represent a high demand in electric vehicles and mobile electronics.[1-5] Intensive studies have proven that the performance of ECs is strongly affected by the morphology and crystal structure of $MnO_2$ that depend on the synthetic strategy and reaction conditions.[6-7] Especially, various crystal structures of $MnO_2$ are classified by the different size of the tunnel, which can deeply influence the electrochemical properties owing to the insertion/extraction of protons or cations into the electroactive materials. For instance, $\alpha$-$MnO_2$ is widely used as the electrode material because of its 2 × 2 tunnels (~ 4.6 Å), which favors the storage of electrolytic cations (such as $Li^+$, $Na^+$, etc.) for their large size, thereby facilitating the ion diffusion and contributing high specific capacitance ($C_{sp}$).[8-10] However, due to the intrinsic poor electrical conductivity of $MnO_2$,[11] and the short diffusion distance (~20 nm) of electrolytes into electrodes,[12] only the surface part of electroactive material can participate in electrochemical charge storage process, thus limiting its specific capacitance and wide application.

To address this problem, an integrated architecture with the combination of two types of metal oxide materials was designed, *i.e.*, core/shell or hierarchical nanostructures. The core within these architectures offers an efficient way of transporting the ions or electrons, while the shell offers either small voids for high ion accessibility with high material density or a higher surface area for greater adsorption of ions.[13-14] Recent investigations have enormous interest in these architectures of materials, which contain one or more materials based on $MnO_2$, for instance, CuO@$MnO_2$, $Co_3O_4$@Au@$MnO_2$, and $NiCo_2O_4$@$MnO_2$, etc.[15-27] However, each of the hierarchical nanostructure is composed of different metal oxide; besides, how much the surface capacitive effects and diffusion-controlled insertion processes contributed to the total capacitance, *i.e.*, the energy storage mechanisms, have not been well understood. Till now, one of the very first studies by Penner *et al*.[28] has demonstrated that the $C_{sp}$ value of the mesoporous $MnO_2$ nanowires reflected true hybrid energy storage contributions from surface capacitive effects (38% of total $C_{sp}$) coupled with diffusion-controlled capacity (62% of total $C_{sp}$). Afterwards, Lee *et al*.[13] have revealed that the storage capacity of hierarchical $M(OH)_2$/$MnO_2$ nanofibril/nanowires array is highly related to the solvents, but their study did not provide very detailed material analysis to elucidate the capacitance contributions about each of the component. Additionally, through the structure evolution of the core/shell or hierarchical architectures along with electrochemical cycling is believed to be beneficial for understanding the mechanism of stability, unfortunately, there has not been sufficiently investigated so far. Up to now, only Alshareef *et al*.[29] exhibited that the improved capacity associated with electrochemical cycling of the $MnO_2$ nanostructures was due to the formation of defective regions embedded in the materials, but they did not explore the structure evolution related to the capacitance change during the cycling test. Thus, a systematic study focused on deeper understanding the

energy storage mechanism of the core/shell architectures, exploring the capacitance contributions of each component and elucidating the evolution of the nanostructures along with electrochemical cycling, is timely and important.

Herein, we have demonstrated a facile hydrothermal preparation of unique isomorphous $MnO_2$@$MnO_2$ core/shell nanostructures. Such unique structure consisteing of an isomorphous layer of $\beta$-$MnO_2$ nanosheets well grown on the surface of $\beta$-$MnO_2$ nanowires deliver an excellent electrochemical performance as supercapacitor materials. We found that the enhanced $C_{sp}$ of the $MnO_2$@$MnO_2$ electrode is largely contributed by the double-layer charging and Faradaic pseudocapacity according to Conway[30] and Dunn's[31-32] method. In addition, it demonstrates an ultralong cycle stability, *i.e.*, nearly 92.2% retention after 20000 cycles. Though directly observeing the structural evolution of the material during the long-term tests by TEM, it is founded that the desirable cycle stability is not simply a result of the unique isomorphous core/shell hierarchical configuration, but also high mechanical stability as well as the better interfacial structures between the $MnO_2$ nanowire core and the ultrathin $MnO_2$ nanosheet shell. Particularly, the defective and disordered regions throughout the whole core/shell architecture are the main cause for the unusual change in $C_{sp}$ along with cycling. Besides, using simulated morphology on the atomic scale, it is demonstrated that the *c*-axis could be the most favorable migration path for $Na^+$, thus leading to the prominent electrochemical performance of $MnO_2$@$MnO_2$ electrode.

## 2. Experimental Section

### 2.1 Synthesis of $MnO_2$ nanowires

$MnO_2$ nanowires were prepared by hydrothermal treatment of aqueous solution of $KMnO_4$. 40 mL of 0.02 M $KMnO_4$ aqueous solution and 0.05 g of PVP were mixed with vigorously magnetic stirring and transferred into a Teflon-lined stainless-steel autoclave (capacity: 50 mL), which was heated at 140℃ for 12 h and then cooled down to room temperature naturally. The products were filtered and washed several times with distilled water and absolute ethanol, and finally dried in vacuum oven at 60℃ for 12 h.

### 2.2 Synthesis of isomorphous $MnO_2$@$MnO_2$ core/shell nanostructures

The isomorphous $MnO_2$@$MnO_2$ core/shell nanostructures were prepared via the same technical route as making $MnO_2$ nanowires before, the difference of which was that 0.05 g of PVP was replaced by 0.05 g of as-obtained $MnO_2$ nanowires, which were introduced as seed crystals. Particularly, all reactants should be transferred into the Teflon-lined stainless-steel autoclave and heated at 140℃ for 12 h too. Because the amount of the product obtained in a batch of synthesis was small, the synthesis processes were repeated several times to get sufficient quantity for the later experiments.

### 2.2 Material Characterizations

As-prepared products were characterized with a D/max-2550 PC X-ray diffractometer (XRD; Rigaku, Cu-Kα radiation), a scanning electron microscope (SEM; S-4800), and a transmission electron microscope (TEM; JEM-2010F) equipped with an energy dispersive X-ray spectrometer (EDS). The mass of electrode materials was weighed on an XS analytical balance (Mettler Toledo; δ = 0.01 mg).

### 2.2 Electrochemical Characterizations

The high purity graphite paper (0.16 mm thick) was used as the current collector, which was cleaned with distilled water and acetone, then and dried and weighed. The $MnO_2$ nanowires or isomorphous $MnO_2$@$MnO_2$ core/shell nanostructures (80 wt %), acetylene black (15 wt %), and poly (tetrafluoroethylene) (5 wt%) were ground in a mortar, and a few drops of N-methylpyrrolidinone was added to form a syrup. It was coated on to the pretreated graphite paper (coating area: 1.5 $cm^2$) and dried at 110 ℃ under vacuum. Coating and drying steps were repeated to get the loading level of the active material close to 0.5 mg $cm^2$. The mass of active materials used in electrode is about ~0.56 mg and ~0.49 mg for $MnO_2$@$MnO_2$ electrode and $MnO_2$ nanowires electrode, respectively. Finally, the electrodes were dried at 110 ℃ under vacuum for 12 h. Electrochemical performances of the as-obtained products were performed on an Autolab (PGSTAT302N potentiostat) using a three-electrode mode in a 0.5 M $Na_2SO_4$ solution within the potential window of approximately -0.2 to 0.8 V. The isomorphous core/shell $MnO_2$@$MnO_2$ nanostructures or pristine $MnO_2$ nanowires was directly used as the working electrode. The reference electrode and counter electrode were a saturated calomel electrode (SCE) and platinum (Pt) foil, respectively. Cycling life tests over 20000 cycles for both the $MnO_2$@$MnO_2$ electrode and $MnO_2$ nanowires electrode were carried at 5 A/g. The $C_{sp}$ (F/g) and current density (A/g) were calculated based on the mass of active materials. EIS measurements were performed by applying an AC voltage with 5 mV amplitude in a frequency range from 0.01 Hz to 100 KHz. All electrochemical experiments were carried out at 25 ±2 ℃.

## 3. Results and Discussion

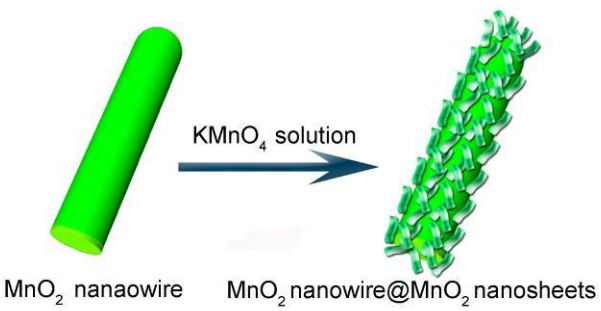


**Scheme 1** The construction of isomorphous $MnO_2$@$MnO_2$ core/shell nanostructure. The green rod represents the $MnO_2$ nanowire backbone, and high light green sheets represent the $MnO_2$ nanosheets.

We proposed the possible growth mechanism of "oriented attachment" and "self-assembly" to demonstrate the construct process for the isomorphous $MnO_2$@$MnO_2$ core/shell nanostructures. In the reaction, as-prepared $MnO_2$ nanowires were acted as the 'substrate', which were added into the $KMnO_4$ solution as seed crystals to direct the self-assembling growth of $MnO_2$ nanosheets in aqueous solution without surfactant and

stabilizers. As shown in Scheme 1, supersaturated solution with a plenty of $MnO_2$ small crystals were formed by adding Mn resource. Because of the high surface energy and thermodynamics instability, $MnO_2$ nuclei can attach to the surface of $MnO_2$ nanowires to decrease surface energy. The crystallographic orientation of the nuclei with respect to each other is determined by the minimization of the highest surface energy. Therefore, with a matching lattice, the lattice fringes' orientation and crystal growth direction are uniform to some extent.[15,33] As reaction time went on, the $MnO_2$ nuclei gradually aggregated and self-assembled to nanosheets. Particularly, the $MnO_2$ nanowires substrate could control the oriented crystallization and self-assembly of $MnO_2$ nanosheets with the same lattice parameters, forming isomorphous $MnO_2$@$MnO_2$ core/shell nanostructures.

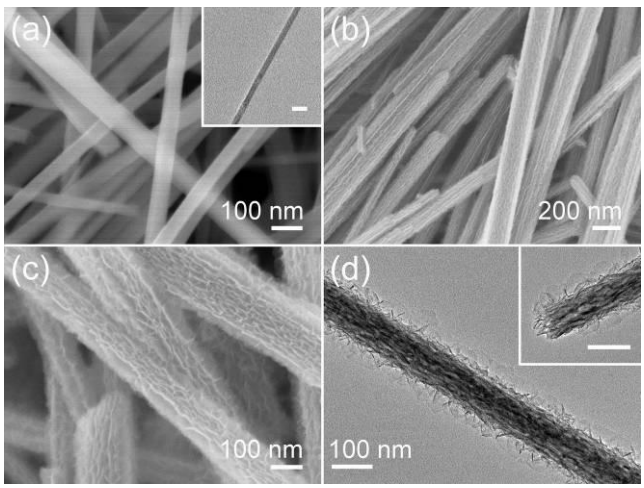


**Fig. 1** (a) SEM image of the $MnO_2$ nanowires, the inset is the TEM image of a single nanowire, scale bar is 100 nm. (b, c) Low and high magnification SEM images of isomorphous $MnO_2$@$MnO_2$ core/shell nanostructure. (d) TEM images of a single isomorphous $MnO_2$@$MnO_2$ core/shell nanostructure, the inset showing the end structure of a nanosheet-coated nanowire, scale bar is 100 nm.

Fig. 1a shows the typical SEM image of freshly prepared pristine $MnO_2$ nanowires, which is in diameter of ~ 50-80 nm and have a smooth surface (inset). A large-scale of as-prepared $MnO_2$ nanowires is shown in Fig. S1 (see ESI†). Fig. 1b is the typical SEM image of isomorphous core/shell $MnO_2$@$MnO_2$ nanostructures. Obviously, no $MnO_2$ is packed in the interspace of the nanowires, suggesting that $MnO_2$ nanosheets are preferentially deposited on the $MnO_2$ nanowires surface. On closer inspection, the surface of $MnO_2$ nanowires are homogenously and adequately covered by ultrathin $MnO_2$ nanosheets, forming a unique core/shell architecture with a highly open and porous structure (Fig. 1c), which can be confirmed by TEM images (Fig. 1d). Clearly, the $MnO_2$ nanowire is tightly bonded and totally covered with thin $MnO_2$ nanosheets. Especially, the nanosheets are interconnected with each other, displaying a high porosity surface morphology, which are highly accessible to electrolytes for energy storage. In addition, a close examination of the exposed profile reveals that each individual architecture is determined to have a diameter of ~150-200 nm (inset of Fig. 1d), larger than the pristine $MnO_2$ nanowires.

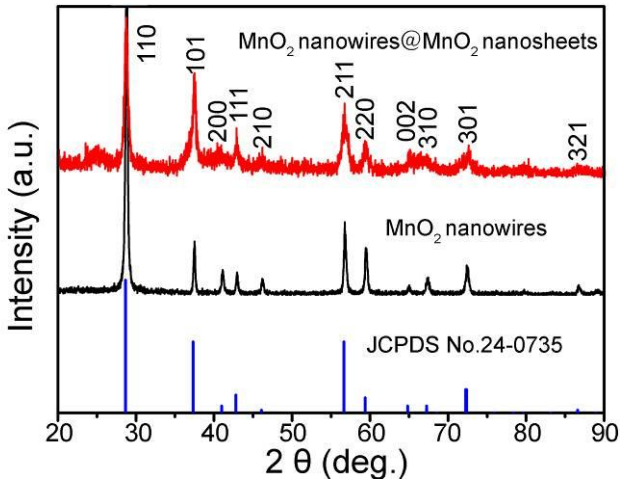


**Fig. 2** XRD pattern of $MnO_2$ nanowires and isomorphous core/shell $MnO_2$@$MnO_2$ nanostructures.

X-ray diffraction (XRD) was carried out to investigate the crystal structure and phase purity of as prepared products. As shown in Fig. 2, it is found that the XRD patterns of pristine $MnO_2$ nanowires confirm the pure phase $\beta$-$MnO_2$ without any other impurities (JCPDS no.24-0735). To our surprise, for the core/shell architectures, the sharp and high intensity peaks also correspond to $\beta$-$MnO_2$, indicating the high purity and crystallinity of the $MnO_2$@$MnO_2$ architecture. Therefore, we can conclude that the shelled nanosheets and the cored nanowires have the same crystal phase, *i.e.*, the final product is isomorphous $MnO_2$ nanowire@$MnO_2$ ultrathin nanosheet core/shell architectures.

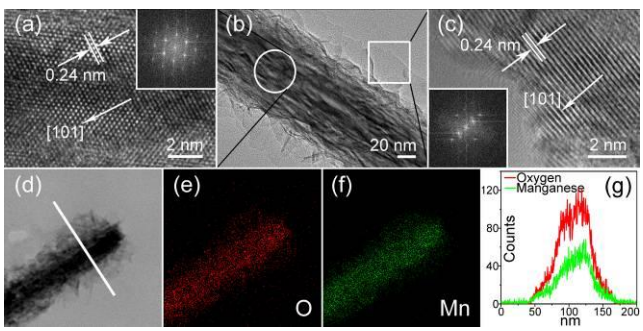


**Fig. 3** (a and c) HRTEM images of an isomorphous $MnO_2$@$MnO_2$ core/shell nanostructure from the circled area and boxed area in (b), respectively; insets corresponding FFT patterns. (b) TEM image of an isomorphous $MnO_2$@$MnO_2$ core/shell nanostructure. (e-f) EDX mapping and spectrum (g) of a single isomorphous $MnO_2$@$MnO_2$ core/shell nanostructure shown in (d).

Fig. 3b shows a typical TEM image of an individual isomorphous $MnO_2$@$MnO_2$ core/shell nanostructue, in which thin nanosheets uniformly cover on the surface of the core $MnO_2$ nanowire. Further analysis of HRTEM image taken from the white circle can clearly see that the lattice fringes with an interplanar spacing of ≈ 0.24 nm, corresponding to the (101) plane of $\beta$-$MnO_2$ crystal (Fig. 3a). The FFT pattern (top-right inset) confirms the single crystal character of this nanowire. Fig. 3c shows the HRTEM image of the nanosheet part within the $MnO_2$@$MnO_2$ nanostructue. By careful inspection, 0.24 nm of *d*-spacing corresponds to the (101) lattice planes, which indicates that the nanosheet favors the [101] growth direction. Moreover, energy-dispersive X-ray spectroscopy (EDX) analysis across

individual core/shel nanowires reveals a distribution of Mn and O elements (Fig. 3e and f). Obviously, the Mn and O signals are detected from the entire structure, verifying that the core/shell is composed of $MnO_2$ nanowire supported $MnO_2$ nanosheets (Fig. 3d). Impressively, the EDX spectrum, unambiguously demonstrated that the $MnO_2$@$MnO_2$ nanowires are composed of Mn and O with Mn/O =1:2 (Fig. 3g). Such an unique structure could improve the ionic transport and mechanical stability.

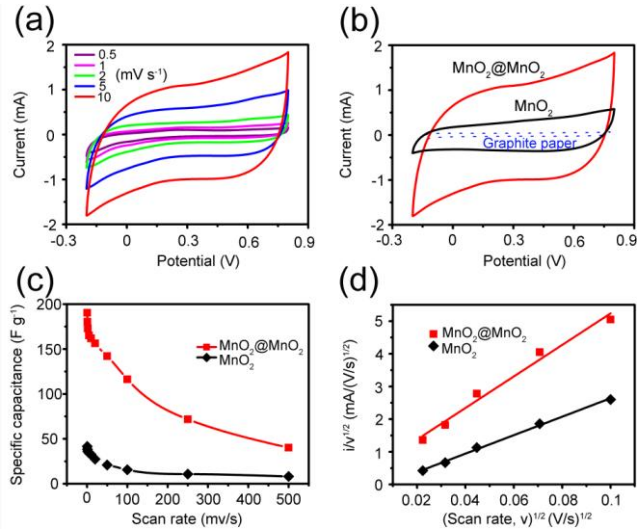


**Fig. 4** (a) CV curves of $MnO_2$@$MnO_2$ electrode. (b) Comparison of CV curves for $MnO_2$@$MnO_2$, $MnO_2$ electrodes and graphite paper at a scan rate of 10 mV/s. (c) Specific capacitances at various scan rates. (d) Use of eq 2 to analyze the voltammetric sweep data for $MnO_2$@$MnO_2$ and $MnO_2$ electrodes, sweep rates varied from 0.5 to 10 mV/s.

As a case study, we used the $MnO_2$@$MnO_2$ electrode to highlight the merits of the isomorphous core/shell nanostructures in ECs applications. We have examined the electrode in a three-electrode configuration with a Pt plate counter electrode and a saturated calomel electrode (SCE) in 0.5 M $Na_2SO_4$ aqueous solution. Fig. 4a shows the cyclic voltammetry (CV) curves of the $MnO_2$@$MnO_2$ electrode at scan rates of 0.5, 1, 2, 5, 10 mV/s with potential windows ranging from -0.2 to 0.8 V. Apparently, the shapes of these curves are quasi-rectangular, indicating fast charging/discharging process at a pseudo-constant rate. In fact, the $MnO_2$ involved redox reactions in the CV tests as the Mn atoms in the overlayers were converted into higher/lower valence states, which were induced by intercalation/extraction of alkali cations ($Na^+$) or protons ($H_3O^+$) into/out of the $MnO_2$@$MnO_2$ core/shell nanostructues and expressed as follow:[34]

$$MnO_2 + M^+ + e^- \leftrightarrow MnOOM \qquad (1)$$
$$M^+ = Na^+ \text{ or } H_3O^+$$

To demonstrate the benefits of the $MnO_2$@$MnO_2$ core/shell nanostructues, the CV curves comparison of the pristine $MnO_2$ nanowires electrode and the $MnO_2$@$MnO_2$ electrode at 10 mV/s are shown in Fig. 4b. Noteworthy, the current of the $MnO_2$@$MnO_2$ electrode is higher than that of $MnO_2$ nanowires electrode, especially the CV integrated area from the graphite paper substrate is negligibly small compare with two electrodes. The apparently increase of CV integrated area indicates that the $MnO_2$@$MnO_2$ electrode have a significantly larger $C_{sp}$ than unitary $MnO_2$ nanowires electrode. The $C_{sp}$ calculated from the CV curves at various scan rates are shown in Fig. 4c (for details, see Fig. S2 in ESI †). Evidently, the $C_{sp}$ of $MnO_2$@$MnO_2$ electrode can achieve 190.5 F/g at 0.5 mV/s, while the $MnO_2$ nanowires electrode is only 41.6 F/g. The summary plot of $C_{sp}$ demonstrates that $MnO_2$@$MnO_2$ electrode yield an enhanced capacitance with 4~5 times than that of the $MnO_2$ nanowires electrode at all scan rates. This larger $C_{sp}$ could be due to both the unique microstructure and the synergetic effect from the ultrathin $MnO_2$ nanosheets (shell) and the $MnO_2$ nanowires (core). The $MnO_2$ nanosheets are well grown and dispersed on the surface of the $MnO_2$ nanowires, creating a highly porous surface morphology, which can provide higher surface area and more active sites for the rapid intercalation and deintercalation of cations ($Na^+$).[15,35]

At an even more fundamental level, these $C_{sp}$ values reflected the true hybrid electrical energy storage with significant contributions from double-layer capacitance and non-inseration pseudocapacitance coupled with a Faradaic insertion capacity. However, these values are appealing but have not completely understood, it is interesting to know how different this charge is stored, whether it is controlled by capacitive elements or diffusion-controlled intercalation elements.

Conway[30] and Dunn[31-32] have demonstrated an elegant method, and recently Penner[28] and Lee[13] used it to quantitatively separate the contribution of the capacitive elements of the charge storage from the diffusion-controlled insertion processes, *i.e.*, by examining the scan rate dependence of the current, the capacitive contributions can be separated from the total stored charge. In principle, three processes contribute to the currents measured for the $MnO_2$ material: (1) double-layer charging of $MnO_2$ surfaces, (2) pseudocapacitive Faradaic current associated with redox reactions of surface $Mn^{3+/4+}$ centers, (3) Faradaic reactions of $Mn^{3+/4+}$ centers requiring $Na^+$ insertion/deinsertion for charge compensation.[28] We can express the current response at a fixed potential as the combination of two separate mechanisms, *i.e.*, surface capacitive effects and diffusion-controlled insertion processes:[30,36]

$$i(V) = k_1 v + k_2 v^{1/2} \qquad (2)$$

For analytical purposes, we divide both side of this equation with the square root of the scan rate, then:

$$i(V)/v^{1/2} = k_1 v^{1/2} + k_2 \quad (3)$$

In eq (2), *i(V)* is the current at a given voltage, *v* is the scan rate, $k_1$ and $k_2$ are scan rate independent constants, $k_1 v$ and $k_2 v^{1/2}$ correspond to the current contributions from the surface capacitive effects and the diffusion-controlled intercalation process, respectively. Then, we plot the scan rate dependence of the current according to eq (3) shown in Fig. 4d. The liner behavior enables us to determine $k_1$ and $k_2$ from the slope and the y-axis intercept point of a straight line at each given voltage, respectively. From this procedure, we are able to distinguish quantitatively between the currents arising from capacitive processes and those occurring from $Na^+$ insertion.

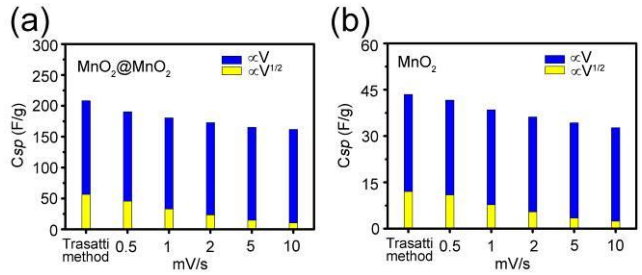


**Fig. 5** Bar graph of $C_{sp}$ of (a) isomorphous $MnO_2$@$MnO_2$ core/shell nanostructures electrode and (b) $MnO_2$ nanowires electrode versus scan rate with Faradaic insertion capacity ($\propto v^{1/2}$, yellow) and double-layer charging and Faradaic pseudocapacity ($\propto v$, blue) derived from Dunn's method and the maximum capacitances derived from Trasatti's method.

Fig. 5 shows the $C_{sp}$ (gravimetrically normalized) and the amounts attributed to the two different charge storage processes (details shown in Table S1). By comparing the double-layer charging and Faradaic pseudocapacity (blue area, $i(v) \propto v$ in Fig. 5a) with the $C_{sp}$, we find that these capacitive effects contributed 76%, 81.7%, 86.4%, 91% and 93.4% of the total capacitance from 0.5 to 10 mV/s, respectively. Clearly, they are significantly higher than those from the Faradaic insertion contribution (yellow area, $i(v) \propto v^{1/2}$ in Fig. 5a). Moreover, the disparity in charge storage for the two different mechanisms becomes more pronounced at higher scan rates because of the rapid charge/discharge characteristics associated with capacitive processes. Besides, the capacitive effects (blue area, $i(v) \propto v$) contributed 73.7%, 79.9%, 84.9%, 89.9% and 92.6% of the total capacitance for the $MnO_2$ nanowires electrode (Fig. 5b), which is similar with the $MnO_2$@$MnO_2$ electrode. Thus, the larger $C_{sp}$ of $MnO_2$@$MnO_2$ electrode mainly comes from an increase in double-layer charging and Faradaic pseudocapacity.

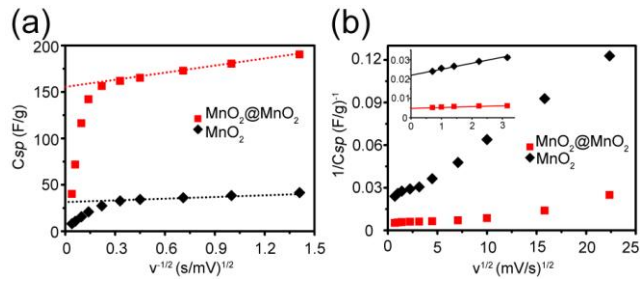


**Fig. 6** (a) $C_{sp}$ versus inverse square root of scan rate and (b) inverse $C_{sp}$ versus square root of scan rate for isomorphous core/shell $MnO_2$@$MnO_2$ nanostructures electrode (red squares) and $MnO_2$ nanowires electrode (black squares), the inset of (b) representing the linear aspect of these points at low scan rates.

Another method was also developed to separate capacitive elements from insertion processes by Trasatti and Lee.[13,37] As can be seen from Fig. 4c, the $C_{sp}$ decreases as scan rate increases, which these date can be plotted versus an appropriate function of $v^{-1/2}$ or $v^{1/2}$ (Fig. 6), the scan rate, with the aim to extrapolate the values of $C_{sp}$ to $v = 0$ and $v = \infty$. If we allowed sufficient time for every reaction to take place, the $C_{sp}$ at 0 mV/s will demonstrate the total capacitance ($C_{tot}$), while the $C_{sp}$ at infinite will give us only the charge stored at the surface ($C_{sur}$). Then the capacitance related to the insertion process ($C_{ins}$) can be obtained from the difference between the total and the surface capacitance ($C_{tot}$-$C_{sur}$).

We get the maximum capacitance related to the surface charges by plotting $C_{sp}$ versus $v^{-1/2}$ for both the $MnO_2$@$MnO_2$ electrode and $MnO_2$ nanowires electrode. We assume there exist a semi-infinite linear diffusion, so we expect a liner correction between $C_{sp}$ and $v^{-1/2}$. In Fig. 6a, the liner can only fit appropriately at low scan rate (0.5 to 10 mV/s) where the points are close to linear. However, it deviates from linearity at high scan rates, which is caused by ohmic drops and irreversible redox transitions due to the resistance of $MnO_2$.[38] From this curve, we can obtain $v^{-1/2} = 0$, which represents the maximum $C_{sur}$ of the material, and the result can be found in Fig. 5a blue areas of the bar graphs labeled "Trasatti Method". In addition, we have plotted the $1/C_{sp}$ versus $v^{1/2}$ (Fig. 6b) and extrapolated the liner at low scan rate, $v^{1/2} = 0$, where we can observe the total maximum capacitance. These results were displayed in Fig. 5 together with the values from Dunn's method at various scan rates. Remarkably, both Trasatti's and Dunn's methods display similar quantitative values with a better correlation at the low scan rate.

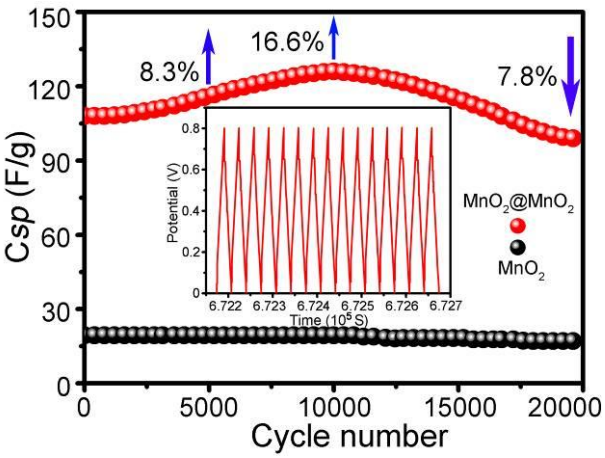


**Fig. 7** Cycling stability of the isomorphous $MnO_2$@$MnO_2$ core/shell nanostructures electrode and $MnO_2$ nanowires electrode. The inset shows the charge-discharge curves of the last 15 cycles for the isomorphous $MnO_2$@$MnO_2$ core/shell nanowires.

Fig. 7 shows the cycling stability of the $MnO_2$@$MnO_2$ electrode and the $MnO_2$ nanowires electrode by conducting charge/discharge tests at a current density of 5 A/g for 20000 cycles. It is interesting to find that the $C_{sp}$ of the $MnO_2$@$MnO_2$ electrode continuouly increases until about 10000 cycles. During the first 5000 cycles, the $C_{sp}$ increases from 108 F/g to 117 F/g, showing 8.3% increase. While the highest $C_{sp}$ (126 F/g) can be obtained at about 10000th cycle, displaying about 16.6% increase. What's more, the $C_{sp}$ based on the $MnO_2$@$MnO_2$ and $MnO_2$ nanowires electrodes retain 92.2% and 88.1% of their initial capacitance after 20000 cycles respectively, demonstrating the $MnO_2$@$MnO_2$ electrode exhibits a higher $C_{sp}$ and cycle stability for such a long term cycling test, as further evident from the very stable charge-discharge curves for the last 15 cycles (the inset image).

Nyquist plots of the $MnO_2$@$MnO_2$ and $MnO_2$ electrodes are shown in Fig. S2d. The less value of equivalent series resistance (*Rs*) for $MnO_2$@$MnO_2$ (2.03 Ω, 3.35 Ω for $MnO_2$ electrode) indicates a good conductivity of the electrolyte and the very low internal resistance of the $MnO_2$@$MnO_2$ core/shell structures. Especially, $MnO_2$@$MnO_2$ core/shell structures has a smaller

charge transfer resistance (*Rct*) value (2.84 Ω) than $MnO_2$ naowires (4.03 Ω), which demonstrates that $MnO_2$ nanosheets are well grown on $MnO_2$ nanowires, providing an ideal pathway for ion and electron transport without kinetic limitations.[39-40] As a result, the $MnO_2$@$MnO_2$ electrode shown the enhanced electrochemical performance among the cycling test. Additionally, the remarkable cycling performance demonstrates the robustness of the isomorphous core/shell nanostructure and the strong integration between the $MnO_2$ cored nanowire and $MnO_2$ shelled nanosheets, which can easily withstand prolonged charge-discharge cycling.

These excellent performances are contributed by the unique design of the isomorphous core/shell $MnO_2$@$MnO_2$ nanostructures which includes the following merits: i) the key advantage of this architecture is the robust mechanical stability. The core and shell are the same crystalline structure pseudocapacitive materials, which would solve the aggregation and volume expansion issues due to the harsh and frequent phase variation during long-term cycling tests. After that, the coll/shell germertry of the isomorphous nanostructures is overall preserved with little structural deformation, as discuss later. This is quite different from the capacitance enhancement by previous hierarchical core/shell nanostructure arrays, such as $Co_3O_4$@$MnO_2$, $NiCo_2O_4$@$MnO_2$, etc,[16,20] *i.e.*, both the core and shell materials are in different crystal form, which would lead to the structural deformation and then destroy the mechanical stability and reduce the electrochemical performance. ii) The ultrathin $MnO_2$ nanosheets are well dispersed on the surface of $MnO_2$ nanowires, constructing a three dimensional (3D) and highly porous structure, making them fully available to the $Na^+$ in the electrolyte. In addition, the entirely exposed nanosheet edges can also facilitate the fast $Na^+$ intercalation into the layered structure; even completely covered, the $MnO_2$ core nanowires can still be accessed by $SO_4^{2-}$ and initiate the redox reaction, thus enhancing the electrochemical kinetics.[35,41]

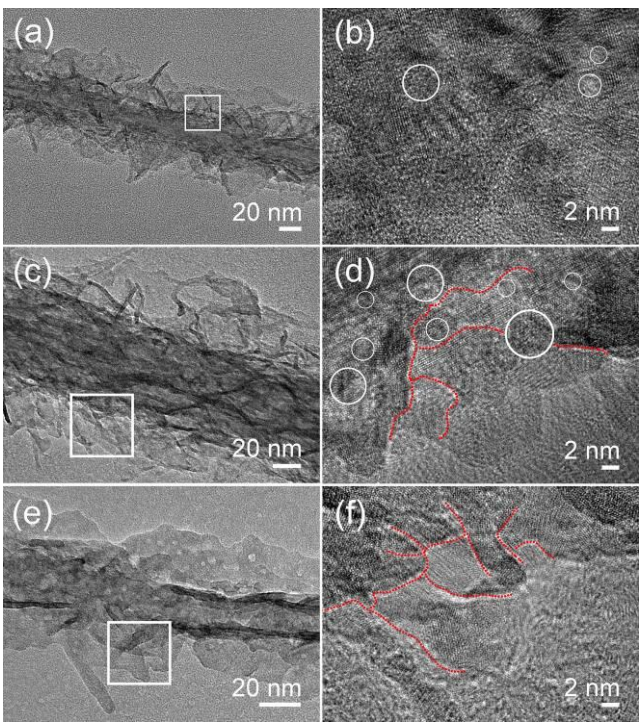


**Fig. 8** TEM images of the isomorphous $MnO_2$@$MnO_2$ core/shell nanostructures after 5000 (a, b), 10000 (c, d) and 20000 (e, f) cycles at different magnifications.

Although the effects of the morphology, crystal phase, and cycling on the supercapacitive performance of those $MnO_2$ related-core/shell nanostructures have been reported previously, the reason of the commonly observed unusual increase in $C_{sp}$ of the $MnO_2$@$MnO_2$ electrode along with cycling is, at present, not fully understood.[34,42] In this section, we have conducted TEM studies to investigate any possible morphological or microstructural changes for the isomorphous core/shell nanostructures caused by the long term cycling tests for the first time. As shown in Fig. 8a, the $MnO_2$ nanosheets on the $MnO_2$ nanowires (core) became rough and irregular after 5000 cycles, while keeping their initial morphological features. Studying closely at some portions of the $MnO_2$ nanosheets (white square area), it is surprised to find that some disordered or defective regions have been formed on the nanosheets (Fig. 8b), which is largely different from the smooth and neat shape of the initial nanosheets (Fig. 3b). The defective regions with small sizes (white circles in Fig. 8b), ranging from 2 to 4 nm in the mesoporous range, demonstrate the disappearance of the crystalline fringes, which are probably caused by the repeated electrolyte ions insertion and extraction upon the cycling tests. Thus, the crystallinity of the regions became poor. After 10000 cycles, many "blooming gaps" were created and deposited closely on the surface of the nanosheets, indicating that the electrode is "corroded". Besides, much more defective or disordered regions are formed throughout the whole core/shell architectures (Fig. 8c). Enlarged view from the area (white square area), a number of small defective sites are clearly shown, the size of which is between 2 and 6 nm (Fig. 8d). Moreover, the high resolution TEM image near the tip portion indicates that the long gaps were formed (red dot curves in Fig. 8d). It is worth pointing out that by repeating electrolyte ions insertion/deinsertion between the electrode materials and electrolytes, the nanosheets are forced to be vertical to the electrode surface in order to shorten the electrolyte ion transportation length, while the pores tend to become larger to facilitate more electrolyte accesses for ion adsorption/desorption or redox reactions.[29] Upon increasing the cycles up to 20000, we are surprised to find that large quantities of pores or voids were formed on the isomorphous core/shell $MnO_2$@$MnO_2$ nanostructures (Fig. 8e). These voids from the disordered regions are in different size and shape mainly due to slow dissolution of $MnO_2$ in the electrolyte, which is caused by the less desirable insertion cations ($Na^+$) compared with the fast $H^+$ insertion process.[2] Impressively, the gaps induced by the electrochemical cycling tests are much more visible, which is largely contributed to the increased reductive-dissolution of the electrode materials associated with the increased access of the electrolyte ions to them. The similar results have been observed by Chen and co-workers, where many voids were formed only after 5000 cycles.[29]

The formation of the defective regions within the isomorphous core/shell $MnO_2$@$MnO_2$ nanostructures upon cycling is attributed to the repeated insertion/deinsertion of the electrolyte ions into/out of the $MnO_2$@$MnO_2$ electrode materials. Firstly, the $C_{sp}$ gradual increase indicates that there is an initial activation

process of the electrodes. Furthermore, with progressive cycling, the defective regions were formed and embedded in the $MnO_2$ nanostructures, resulting in increased porosity, surface area, and consequently increased electrochemical capacity in varying degrees. However, after such long-term electrochemical cycling tests, the $MnO_2$@$MnO_2$ electrode materials was suffered a gradually reductive-dissolution process in the electrolytes, thus making the $C_{sp}$ decrease eventually. Besides, the ultralong cycle stability is not simply a result of the unique isomorphous core/shell nanostructures that using the same material, as this configuration may have better interfacial structures but not overall mechanical stability. Using *in-situ* TEM, Gu *et al*. had demonstrated that the conductive polymer-Si anode exhibited superior electrochemical cycling stability mainly due to the resilient bonding between the conductive polymer and Si nanoparticles.[43] Meanwile, because of the strongly adhesion between amorphous silicon and carbon nanofiber , no spallation or cracking is observed during the cyclic test, thus making an enhanced cycling stability of the composite anode in Wang's report.[44] It can be generally realized that the thickness of layer and possibly the unique isomorphous nanostructures as well as the interfacial structures between the core and shell can become design parameters to optimize the lifetime of electrode based on transition metal oxides.

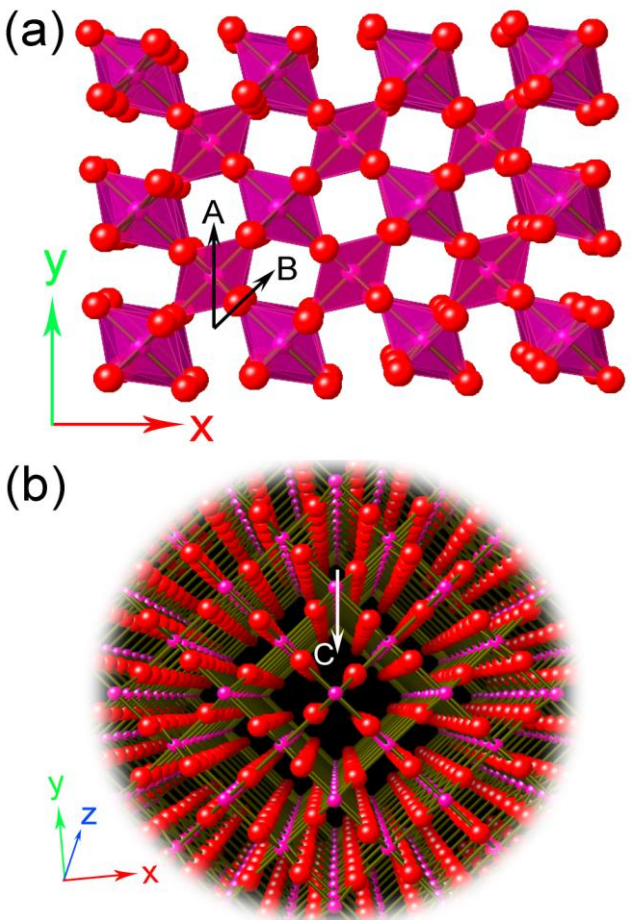


**Fig. 9** Crystal structure of the connected $MnO_6$ octahedra and the intercalated alkali ions for $\beta$-$MnO_2$ viewed along the c-axis (a) and obliquely (b). Red spheres are oxygen, and purple are manganese. Migration paths are indicated by bold arrows. (a) Polyhedral model; (b) ball & stick model.

$\beta$-$MnO_2$ has been extensively investigated as a cathode for ECs because of its thermodynamically stable phase,[45] but early work showed lower capacitance than other polymorphs such as hollandite $MnO_2$.[32] Devaraj *et al*. had demonstrated that the narrow tunnel size (1.89 Å) prevents the cations from inserting into $\beta$-$MnO_2$, thus resulted in the low $C_{sp}$. However, in our work, the isomorphous $MnO_2$@$MnO_2$ core/shell nanostructures show a higher capacitance than that of $MnO_2$ nanowires and also exhibit excellent stability after 20000 cycles. Motivated by the dramatically difference, we performed a study using simulated morphology to investigate the related question on the atomic scale.

Fig. 9 shows the crystal structure of $\beta$-$MnO_2$ where the approximate $MnO_6$ octahedras are indicated by polyhedral. We exhibit three probable paths for migration of alkali ions in the dilute limit of bulk $\beta$-$MnO_2$. Path A corresponds to migration in *a*, *b*-plane (along [010] and symmetry equivalent [100]). Path B is migration simultaneously along *c*-axis and in the *a*,*b*-plane (along [111] and symmetry equivalent paths). Path C is migration along 1×1 *c*-axis tunnel (directed along [001], Fig. 9b, details are in Fig. S3). According to Saiful *et al*.'s work,[46] we consider that the path C (*c*-axis) is the most favorable path becaue paths A and B possess very high migration barriers due to the migration between the *c*-axis tunnels requires large distortion of the $MnO_6$ octahedra as well as a large energy cost. In addition, to assess the surface to bulk migration barrier, the (001) surface has the lowest energy, and then is (101). As shown in Fig. 3, the $MnO_2$ nanosheets expose the (101) plane, which is in favor of the $Na^+$ migration from the surface to bulk of $MnO_2$ material and enhance intercalation process. However, the Faradaic insertion capacitive effects (yellow area, $i(v) \propto v^{1/2}$ in Fig. 5a) contributed to the total capacitance are significantly lower than those from the double-layer charging and Faradaic pseudocapacity (blue area, $i(v) \propto v$ in Fig. 5a). The availability of only narrow one-dimensional channels for sodium-ion diffusion, makes $\beta$-$MnO_2$ unsuitable as an insertion electrode for supercapacitors even in lithium batteries, for instance, a highly crystalline $\beta$-$MnO_2$ structure can accommodate only 0.2 $Li^+$ ions at room temperature.[47] In our experiments, the high specific capacitance performance of $MnO_2$@$MnO_2$ electrode mainly can be attributed to the unique core/shell architecture with a highly open and porous structure (Fig. 1c,d), which offer large electrochemically accessible surface areasfor charge transfer and reduce ion diffusion distance during the charge/discharge process, thus displaying excelent electrochemical performance.

## 4. Conclusions

In summmary, we have carried out an extensive study of hydrothermally-derived isomorphous $MnO_2$@$MnO_2$ core/shell nanostructures, which are consists of an isomorphous layer of $\beta$-$MnO_2$ nanosheets (shell) well grown on the surface of $\beta$-$MnO_2$ nanowires (core). As a model example, the smart electrode made of the isomorphous $MnO_2$@$MnO_2$ core/shell nanostructures delivers remarkable electrochemical performance, *i.e.*, yielding greatly improved $C_{sp}$ with 4~5 times higher than that of $MnO_2$ nanowires (190.5 F/g *vs.* 41.6 F/g). Moreover, we have proved that the increased $C_{sp}$ of the $MnO_2$@$MnO_2$ electrode is largely contributed by the capacitive processes including double-layer

charging and Faradaic pseudocapacity from Conway and Dunn's method. In addition, it also demonstrates an desirable cycle stability, *i.e.*, nearly 92.2% retention after 20000 cycles at a current density of 5 A/g. Such intriguing capacitive behavior is attributed to the unique isomorphous core/shell hierarchical configuration and high mechanical stability as well as the better interfacial structures between the $MnO_2$ nanowire core and the ultrathin $MnO_2$ nanosheet shell. Furthermore, the defective and disordered regions throughout the whole core/shell architectures are the main cause for the unusual change in $C_{sp}$ along with cycling, by direct observation of the structural evolution of the involved material during the tests. Particularly, using simulated morphology on the atomic scale, the *c*-axis could be the most favorable migration path for $Na^+$, leading to the isomorphous $MnO_2$@$MnO_2$ core/shell nanostructures exhibit an excellent electrochemical performance. Such comprehensive study may provide potential directions for the design of the materials that used in many different applications where $MnO_2$ is already or proposed to be employed.

## Acknowledgements

This work was financially supported by the NSFC (21171035, 51472049, 51302035), the Key Grant Project of Chinese Ministry of Education (313015), the PhD Programs Foundation of the Ministry of Education of China (20110075110008, 20130075120001), the National 863 Program of China (2013AA031903), the Science and Technology Commission of Shanghai Municipality (13ZR1451200), the Fundamental Research Funds for the Central Universities, the Program Innovative Research Team in University (IRT1221), the Shanghai Leading Academic Discipline Project (B603) and the Program of Introducing Talents of Discipline to Universities (111-2-04), the graduate students scientific research innovation projects of Shanghai university of engineering science (14KY0512), the 2012 special fund of development of science and technology of Shanghai university of engineering science (2013gp19).

## Notes and references

[a]*School of material engineering, Shanghai university of engineering science, Shanghai 201620, China.*
*E-mail: xiyingzhou@yahoo.com; liwenyao314@gmail.com;*
[b]*State Key Laboratory for Modification of Chemical Fibers and Polymer Materials, College of Materials Science and Engineering, Donghua University, Shanghai 201620, China.*
*E-mail: hu.junqing@dhu.edu.cn;*
[c]*Center of Super-Diamond and Advanced Films (COSDAF), Department of Physics and Materials Science, City University of Hong Kong, Hong Kong.*

† Electronic Supplementary Information (ESI) available: [Experimental process, Supplementary Fig.s and Specific capacitance calculation]. See DOI: 10.1039/b000000x/

1 P. Simon, Y. Gogotsi, *Nat. Mater.* 2008, **7**, 845.
2 W. Wei, X. Cui, W. Chen and D. G. Ivey, *Chem. Soc. Rev.*, 2011, **40**, 1697.
3 G. Wang, L. Zhang and J. Zhang, *Chem. Soc. Rev.*, 2012, **41**, 797.
4 H. Wang, L.-F. Cui, Y. Yang, H. S. Casalongue, J. T. Robinson, Y. Liang, Y. Cui and H. Dai, *J. Am. Chem. Soc.*, 2010, **132**, 13978.
5 A. L. M. Reddy, M. M. Shaijumon, S. R. Gowda and P. M. Ajayan, *Nano Lett.*, 2009, **9**, 1002.
6 S. Devaraj and N. Munichandraiah, *J. Phys. Chem. C*, 2008, **112**, 4406-4417.
7 T. T. Truong, Y. Liu, Y. Ren, L. Trahey and Y. Sun, *ACS Nano*, 2012, **6**, 8067.
8 S. L. Brock, N. G. Duan, Z. R. Tian, O. Giraldo, H. Zhou and S. L. Suib, *Chem. Mater.*, 1998, **10**, 2619.
9 R. H. Ma, Y. Bando, L. Q. Zhang and T. Sasaki, *Adv. Mater.*, 2004, **16**, 918..
10 R. N. Reddy and R. G. Reddy, *J. Power Sources*, 2003, **124**, 330.
11 Z. Yu, B. Duong, D. Abbitt and J. Thomas, *Adv. Mater.*, 2013, **25**, 3302.
12 C. C. Hu, K. H. Chang, M. C. Lin and Y. T. Wu, *Nano Lett.*, 2006, **6**, 2690.
13 J. Duay, S. A. Sherrill, Z. Gui, E. Gillette and S. B. Lee, *ACS Nano*, 2013, **7**, 1200.
14 L. Su, Y. Jing and Z. Zhou, *Nanoscale*, 2011, **3**, 3967.
15 M. Huang, Y. Zhang, F. Li, Z. Wang, Alamusi, N. Hu, Z. Wen and Q. Liu, *Sci. Rep.*, 2014, **4**, 4518.
16 H. Xia, D. Zhu, Z. Luo, Y. Yu, X. Shi, G. Yuan and J. Xie, *Sci. Rep.*, 2013, **3**, 1.
17 W. Li, G. Li, J. Sun, R. Zou, K. Xu, Y. Sun, Z. Chen, J. Yang and J. Hu, *Nanoscale*, 2013, **5**, 2901.
18 X. Sun, Q. Li, Y. Lu and Y. Mao, *Chem. Commun.*, 2013, **49**, 4456.
19 L. Yu, G. Zhang, C. Yuan and X. W. Lou, *Chem. Commun.*, 2013, **49**, 137.
20 Q. Li, Z. L. Wang, G. R. Li, R. Guo, L. X. Ding and Y. X. Tong, *Nano Lett.*, 2012, **12**, 3803.
21 A. Magasinski, P. Dixon, B. Hertzberg, A. Kvit, J. Ayala and G. Yushin, *Nat. Mater.*, 2010, **9**, 353.
22 L. Bao, J. Zang and X. Li, *Nano Lett.*, 2011, **11**, 1215.
23 H. Y. Wang, F. X. Xiao, L. Yu, B. Liu and X. W. Lou, *Small*, 2014, **10**, 3181.
24 L. F. Chen, Z. H. Huang, H. W. Liang, Q. F. Guan and S. H. Yu, *Adv. Mater.*, 2013, **25**, 4746.
25 S. Wang, B. Pei, X. Zhao and R. A. W. Dryfe, *Nano Energy*, 2013, **2**, 530.
26 L. F. Chen, Z. Y. Yu, X. Ma, Z. Y. Li and S. H. Yu, *Nano Energy*, 2014, **9**, 345.
27 Z. Y. Yu, L. F. Chen and S. H. Yu, *J. Mater. Chem. A*, 2014, **2**, 10889.
28 W. Yan, T. Ayvazian, J. Kim, Y. Liu, K. C. Donavan, W. Xing, Y. Yang, J. C. Hemminger and R. M. Penner, *ACS Nano*, 2011, **5**, 8275.
29 W. Chen, R. B. Rakhi, Q. Wang, M. N. Hedhili and H. N. Alshareef, *Adv. Func. Mater.*, 2014, **24**, 3130.
30 W. G. P. T. C. Liu, and B. E. Conway and S. L. Roberson, *J. Electrochem. Soc.*, 1998, **145**, 1882.
31 K. Brezesinski, J. Wang, J. Haetge, C. Reitz, S. O. Steinmueller, S. H. Tolbert, B. M. Smarsly, B. Dunn and T. Brezesinski, *J. Am. Chem. Soc.*, 2010, **132**, 6982.
32 J. Wang, J. Polleux, J. Lim and B. Dunn, *J. Phys. Chem. C*, 2007, **111**, 14925.
33 L. Q. Mai, F. Yang, Y. L. Zhao, X. Xu, L. Xu and Y. Z. Luo, *Nat. Commun.*, 2011, **2**, 381.
34 M. Toupin, T. Brousse and D. Belanger, *Chem. Mater.*, 2004, **16**, 3184.
35 Y. Luo, D. Kong, J. Luo, S. Chen, D. Zhang, K. Qiu, X. Qi, H. Zhang, C. M. Li and T. Yu, *RSC Adv.*, 2013, **3**, 14413.
36 T. Brezesinski, J. Wang, J. Polleux, B. Dunn and S. H. Tolbert, *J. Am. Chem. Soc.*, 2009, **131**, 1802.
37 S. Ardizzone, G. Fregonara and S. Trasatti, *Electrochim. Acta*, 1990, **35**, 263.
38 C. P. Depauli and S. Trasatti, *J. Electroanal. Chem.*, 1995, **396**, 161.
39 L. Su, Z. Zhou and M. Ren, *Chem. Commun.*, 2010, **46**, 2590.
40 L. Su, Y. Zhong, J. Wei and Z. Zhou, *RSC Adv.*, 2013, **3**, 9035.
41 J. Liu, J. Jiang, C. Cheng, H. Li, J. Zhang, H. Gong and H. J. Fan, *Adv. Mater.*, 2011, **23**, 2076.
42 K. Xu, W. Li, Q. Liu, B. Li, X. Liu, L. An, Z. Chen, R. Zou and J. Hu, *J. Mater. Chem. A*, 2014, **2**, 4795.
43 M. Gu, X. C. Xiao, G. Liu, S. Thevuthasan, D. R. Baer, J. G. Zhang, J. Liu, N. D. Browning and C. M. Wang, *Sci. Rep.*, 2014, **4**, 3684.

44 C. M. Wang, X. Li, Z. Wang, W. Xu, J. Liu, F. Gao, L. Kovarik, J. G. Zhang, J. Howe, D. J. Burton, Z. Liu, X. Xiao, S. Thevuthasan and D. R. Baer, *Nano Lett.*, 2012, **12**, 1624.
45 F. Cheng, T. Zhang, Y. Zhang, J. Du, X. Han and J. Chen, *Angew. Chem. Int. Ed.*, 2013, **52**, 2474.
46 D. A. Tompsett, S. C. Parker, P. G. Bruce and M. S. Islam, *Chem. Mater.*, 2013, **25**, 536.
47 D.W. Murphy, F.J. Di Salvo, J.N. Carides and J.V. Waszczak, *Mat. Res. Bull.*, 1978, **13**, 1395.

## The table of contents entry

The isomorphous $MnO_2$@$MnO_2$ core/shell nanostructures through a facial hydrothermal process resulted in remarkable electrochemical performances, *i.e.*, a high specific capacitance with excellent cycling stability (92.2% retention after 20000 cycles), in which the defective and disordered regions observed whin the core/shell architectures are the main cause for the unusual change in $C_{sp}$ along with cycling.